Title
Broad-band trajectory mechanics

Journal
Geophysical Journal International, 216(2)

ISSN
0956-540X

Authors
Vasco, DW
Nihei, Kurt

Publication Date
2019

DOI
10.1093/gji/ggy435

Peer reviewed

submitted to *Geophys. J. Int.*

Broad band trajectory mechanics

D. W. Vasco and Kurt Nihei

Lawrence Berkeley National Laboratory,

University of California,

Berkeley, California 94720

SUMMARY

We present a trajectory-based solution to the elasto-dynamic equation of motion that is valid across a wide range of seismic frequencies. That is, the derivation of the solution does not invoke a high frequency assumption or require that the medium have smoothly-varying properties. The approach, adopted from techniques used in quantum dynamics, produces a set of coupled ordinary differential equations for the trajectory, the slowness vector, and the elastic wave amplitude along the ray path. The trajectories may be determined by a direct solution of the governing equations or derived as the by-product of a numerical wavefield simulation. Synthetic tests with interfaces and layers containing increasingly narrow transition zones indicates that the conventional high-frequency trajectories associated with the eikonal equation bend too sharply into high velocity regions as the wavelength exceeds the transition zone width. Tests in a velocity model, based upon mapped structural surfaces from the Geysers geothermal field in California, indicates that discrepancies between high-frequency and broad band trajectories can exceed several hundred meters at wavelengths of 1 Hz. An application to a crosswell tomographic imaging experiment demonstrates that the technique provides a basis for the seismic monitoring of fluid flow along narrow features such as fracture zones.

Key words: Seismic wave propagation, seismic tomography, seismic imaging, ray methods, high-frequency wave propagation

1 INTRODUCTION

Ray-based methods have proven useful in seismology for both visualizing wave propagation and for efficient tomographic inversions based upon seismic first arrival times (Aki et al. 1976, Iyer and Hirahara 1993). Applications of the latter have been widespread, from crosswell tomography (as in Dines and Lytle 1979, McMechan 1983, Peterson et al. 1985), regional earthquake studies (Aki and Lee 1976, Thurber 1983, Serretti and Morelli 2011, etc.), to whole Earth imaging (as in Sengupta and Toksoz 1976, Dziewonski et al. 1977, Hager and Clayton 1989, Inoue et al. 1990, Pulliam et al. 1993, Bijwaard and Spakman 2000, Vasco et al. 2003 and others). While there have been tremendous advances in full waveform inversion, imaging based upon first arrival times is still very useful for deriving a velocity model. The utility is due, in large part, to the quasi-linearity of the inverse problem associated with travel times. That is, tomography based on arrival times is not as sensitive to the initial or starting velocity model as is waveform inversion. Intuitively, the misfit derived from oscillatory waveforms varies in a quasi-periodic fashion in response to lateral shifts of the traces and this generates local minima in the misfit functional (Dessa and Pascal 2003, Alkhalifah and Choi 2012, Bharadwaj et al. 2016). In addition, travel time tomography typically involves much less computation and data handling then does waveform inversion. The determination and use of a first arrival time is a form of data reduction, leading to a much smaller and more tractable inverse problem. Therefore, travel time tomography still has a place in the field of seismic imaging.

Conventional ray-based approaches have their foundation in asymptotic ray theory as described in Karal and Keller (1959), Aki and Richards (1980), Chapman (2004), a technique that was developed earlier as a means to relate electromagnetic wave propagation and geometrical optics (Luneburg 1966, Kline and Kay 1965). The approach explores wave propagation in the limit as the frequency becomes large, or equivalently, for spatial variations in elastic properties that are smooth with respect to the wavelength of the seismic wave (Aki and Richards 1980, p. 89). In such cases, the governing equations for the phase and amplitude of the wave decouple and it is possible to relate perturbations in the travel time directly to perturbations in the elastic properties. Specifically, the variations in the phase of a transient pulse, and of the travel time, may be interpreted in terms of an eikonal equation that only depends upon the seismic velocity. The characteristic ordinary differential equations that are equivalent to the eikonal equation produce expressions for the raypath tangent vector and the slowness vector. Efficient numerical algorithms, based upon finite differences, have also been developed to solve the eikonal equation directly such as papers by Vidale (1988), Sethian (1999), Osher and Fedkiw (2003).

While ray-based methods have proven highly successful, in many situations the conditions for their validity are likely to be violated within the Earth. Elastic properties vary over a wide range of scales in the subsurface and heterogeneity abounds. Such variation is evident in sonic logs that record the spatial variations in compressional velocity along the length of wells (Leary 1991, Holliger 1996, Savran and Olsen 2016). Interfaces, layering, and fracture zones are examples of common structures where material properties can change abruptly. Even at the global scale there are features such as subducting slabs, narrow plumes, and sharp phase transitions where velocities vary over scales that may be shorter than the length scale of some of the longer period waves used to study them. This is particularly true for surface waves that interact with structural features at or near the Earth's surface (Lin and Ritzwoller 2011). Wavelength dependent velocity smoothing (Lomax 1994, Lomax and Snieder 1996, Zelt and Chen 2016) may be used to mitigate deficiencies of high-frequency asymptotic methods but such approaches involve some ad-hoc choices regarding the type of averaging to incorporate.

Following an approach developed in quantum dynamics (Wyatt 2005, Bittner et al. 2010, Bensey et al. 2014, Gu and Garashchuk 2016), we derive a trajectory-based solution to the elastodynamic equation of motion. We do not invoke a high-frequency assumption nor do we assume that the medium is smoothly-varying in comparison to the length scale of the seismic wave. The technique is suitable for modeling first arrival times associated with coherent compressional waves. The set of ordinary differential equations describing the trajectory and the amplitude of the propagating wave are similar to those of asymptotic ray theory. The primary difference is the presence of a term, known as the wave potential, that couples the phase to the amplitude of the wave. The differential equations for the extended solution may be solved using numerial techniques or by a hybrid approach whereby the travel time field is obtained from a numerical solution of the wave equation and the path is obtained by marching down the gradient of the phase field. The latter approach is direct, easy to implement, and stable but does require a forward calculation of the wavefield. We use the wavefield-based algorithm to calculate extended trajectories for several examples involving interfaces and layers with increasingly sharp boundaries. We compare these paths to conventional high-frequency paths derived using the eikonal equation. We also illustrate how the approach can be used for tomographic imaging, providing semi-analytic expressions relating travel time perturbations to small changes in slowness along the trajectory. This allows for easily computed model parameter sensitivities that can be used to extend conventional ray-based methods to models with rapid spatial variations in properties.

2 METHODOLOGY

Our starting point is the elasto-dynamic equation of motion

$$\rho\ddot{\mathbf{u}} = \nabla\left(\lambda\nabla\cdot\mathbf{u}\right) + \nabla\cdot\mu\left[\nabla\mathbf{u} + (\nabla\mathbf{u})^t\right] \tag{1}$$

where $\lambda(\mathbf{x})$ is the Lame parameter, $\mu(\mathbf{x})$ is the shear modulus, and $\rho(\mathbf{x})$ is the density. In this initial application of the technique we shall only consider wave propagation in an isotropic medium without attenuation. Applying the Fourier transform to equation (1) in order to work in the frequency domain results in

$$-\rho\omega^2\mathbf{U} = \nabla\left(\lambda\nabla\cdot\mathbf{U}\right) + \nabla\cdot\mu\left[\nabla\mathbf{U} + (\nabla\mathbf{U})^t\right], \tag{2}$$

where $\mathbf{U}(\mathbf{x},\omega)$ is the transformed displacement vector. Our interest will be in the interpretation of arrivals that are observed at some distance from the source. We assume that the displacements are due to a coherent body wave propagating through the medium. One can write the complex vector $\mathbf{U}(\mathbf{x},\omega)$ in a polar form

$$\mathbf{U}(\mathbf{x},\omega) = \mathbf{R}(\mathbf{x},\omega)e^{-i\varphi(\mathbf{x},\omega)} \tag{3}$$

where $\mathbf{R}(\mathbf{x},\omega)$ and $\varphi(\mathbf{x},\omega)$ are both real variables. Note that the form (3) does not extend to interface waves, including surface waves, where there may be a phase shift between individual components. As shown in the Appendix, substituting the polar form (3) into equation (2) produces an expression containing real and imaginary terms.

2.1 Real terms and the ray equations

As indicated in the Appendix, if we just consider the real terms we arrive at the equation

$$\left(\lambda+\mu\right)\nabla\varphi\cdot\mathbf{R}\nabla\varphi + \mu\nabla\varphi\cdot\nabla\varphi\mathbf{R} - \rho\omega^2\mathbf{R} = \mathbf{F}(\mathbf{x},\omega) \tag{4}$$

where the right-hand-side $\mathbf{F}(\mathbf{x})$ is given by

$$\mathbf{F}(\mathbf{x},\omega) = \left(\nabla\cdot\mathbf{R}\right)\nabla\lambda + \nabla\cdot\mu\left[\nabla\mathbf{R} + (\nabla\mathbf{R})^t\right]. \tag{5}$$

For brevity, we define the wave number vector

$$\mathbf{k} = \nabla\varphi \tag{6}$$

the gradient of the phase function, and the related slowness vector

$$\mathbf{p} = \frac{\mathbf{k}}{\omega} \tag{7}$$

where $\mathbf{p} = \nabla T$ is the gradient of the travel time field $T(\mathbf{x}, \omega)$. Note that this, along with equations (6) and (7), implies that $\varphi(\mathbf{x}, \omega) = \omega T(\mathbf{x}, \omega)$. Equation (4) can be expressed in terms of $\mathbf{k}$ and $\mathbf{R}$

$$(\lambda + \mu)\, \mathbf{k} \cdot \mathbf{R}\mathbf{k} + \mu\mathbf{k} \cdot \mathbf{k}\mathbf{R} - \rho\omega^2\mathbf{R} = \mathbf{F}(\mathbf{x}, \omega). \tag{8}$$

Taking the scalar product of both sides of equation (8) with the displacement vector $\mathbf{R}$ results in single equation in $\mathbf{R}$ and $\mathbf{k}$,

$$(\lambda + \mu)\,(\mathbf{k} \cdot \mathbf{R})^2 + \mu\mathbf{k} \cdot \mathbf{k}R^2 - \rho\omega^2 R^2 = \mathbf{F} \cdot \mathbf{R} \tag{9}$$

where

$$R^2 = \mathbf{R} \cdot \mathbf{R}. \tag{10}$$

Dividing by ρ, ω^2, and R^2, we can write equation (9) in terms of the slowness vector $\mathbf{p}$

$$\alpha^2 \left(\mathbf{p} \cdot \hat{\mathbf{R}}\right)^2 + \beta^2\mathbf{p} \cdot \mathbf{p} - 1 = W(\mathbf{x}, \omega) \tag{11}$$

where

$$\alpha(\mathbf{x}) = \sqrt{\frac{\lambda + \mu}{\rho}}, \tag{12}$$

$$\beta(\mathbf{x}) = \sqrt{\frac{\mu}{\rho}}, \tag{13}$$

$$W(\mathbf{x}, \omega) = \frac{1}{\rho R\omega^2}\mathbf{F} \cdot \hat{\mathbf{R}}, \tag{14}$$

a term that is known as the wave potential, and $\hat{\mathbf{R}}$ is a unit vector in the direction of $\mathbf{R}$. We can write equation (11) as the vanishing of a Hamiltonian function of $\mathbf{x}$ and $\mathbf{p}$, parameterized by ω,

$$H(\mathbf{x}, \mathbf{p}, \omega) = 0 \tag{15}$$

where the Hamiltonian is given by

$$H(\mathbf{x}, \mathbf{p}, \omega) = \alpha^2 \left(\mathbf{p} \cdot \hat{\mathbf{R}}\right)^2 + \beta^2\mathbf{p} \cdot \mathbf{p} - 1 - W(\mathbf{x}, \omega). \tag{16}$$

In a medium with smoothly-varying properties, or at a high enough frequency, the $1/\omega^2$ factor in equation (14) can make the term $W(\mathbf{x}, \omega)$ negligible.

We are interested in the path of a segment of a propagating wavefront as it moves through an elastic medium. To this end, we consider a trajectory $\mathbf{x}(s)$ that denotes the movement of the disturbance from a source location to a given observation point. The parameter s signifies the position along the trajectory and may represent the path length or the travel time. Similarly, we consider the slowness vector to be a function of distance along the path $\mathbf{p}(s)$. Differentiating equation (16) with respect s

$$\frac{dH}{ds} = \nabla_{\mathbf{x}} H \cdot \frac{d\mathbf{x}}{ds} + \nabla_{\mathbf{p}} H \cdot \frac{d\mathbf{p}}{ds} = 0, \tag{17}$$

where we treat the components of $\mathbf{x}$ and $\mathbf{p}$ as variables while ω is considered to be a parameter. Here, $\nabla_{\mathbf{x}}$ signifies the spatial gradient and $\nabla_{\mathbf{p}}$ signifies a gradient with respect to the components of the slowness vector $\mathbf{p}$. Intuitively, equation (17) can be thought of as an orthogonality condition on the six-dimensional vector $(d\mathbf{x}/ds, d\mathbf{p}/ds)$ with respect to the gradient vector $(\nabla_{\mathbf{x}} H, \nabla_{\mathbf{p}} H)$. The orthogonality condition for these two vectors provides the bi-characteristic ordinary differential equations for the trajectory

$$\frac{d\mathbf{x}}{ds} = \nabla_{\mathbf{p}} H = 2\alpha^2 \left(\mathbf{p} \cdot \hat{\mathbf{R}}\right) \hat{\mathbf{R}} + 2\beta^2 \mathbf{p} \tag{18}$$

$$\frac{d\mathbf{p}}{ds} = -\nabla_{\mathbf{x}} H = -\nabla_{\mathbf{x}} \gamma^2 - p^2 \nabla_{\mathbf{x}} \beta^2 + \nabla_{\mathbf{x}} W, \tag{19}$$

where we have defined

$$\gamma = \alpha \left(\mathbf{p} \cdot \hat{\mathbf{R}}\right)$$

and $p^2 = \mathbf{p} \cdot \mathbf{p}$ is the squared magnitude of the wave number vector. These are Hamilton's equations for the conjugate quantities associated with the Hamiltonian (16). Perhaps the most useful form is in terms of the travel time along the trajectory, T, and later we shall write the equations using T to denote position along the path. The equations are generalizations of the expressions associated with a high-frequency asymptotic approximation (Chapman 2004). One important difference is the presence of the function $W(\mathbf{x}, \omega)$ that couples the trajectory to the wave amplitude.

2.2 Expressions for the compressional and shear modes of propagation

Equations (18) and (19) do not distinguish between shear and compressional modes of propagation. That is to be expected because the modes couple at sharp boundaries and the equations must be general enough to describe this. However, in many cases we are interested in the first arriving energy that has propagated solely as a compressional wave. Alternatively, one may wish to focus on arrivals associated with waves that traveled from the source to a given receiver entirely as shear modes. In such cases it is useful to restrict equations (18) and (19) to specific phases that have maintained their identity throughout their journey. Therefore, we shall consider the compressional mode of propagation whereby the particle motion is in the direction of propagation and the shear mode where such motion is perpendicular to this direction.

For the compressional wave in an isotropic and non-attenuating medium the displacement vector is parallel to the propagation direction and we can write the amplitude vector $\mathbf{R}(\mathbf{x},\omega)$ as

$$\mathbf{R}(\mathbf{x},\omega) = R(\mathbf{x},\omega)\hat{\mathbf{p}}(\mathbf{x},\omega) \tag{20}$$

where $\hat{\mathbf{p}}$ is a unit vector in the direction of $\mathbf{p}$. Because $\mathbf{p} = \nabla\varphi$, this restriction is related to the assumption that the wavefield may be derived from a potential function. Equation (20) requires that $\hat{\mathbf{R}} = \hat{\mathbf{p}}$, so that the equations (18) and (19) for the trajectory $\mathbf{x}$ and slowness vector $\mathbf{p}$ reduce to

$$\frac{d\mathbf{x}}{ds} = 2{V_p}^2\mathbf{p} \tag{21}$$

$$\frac{d\mathbf{p}}{ds} = -p^2\nabla_{\mathbf{x}}{V_p}^2 + \nabla_{\mathbf{x}}W, \tag{22}$$

where V_p signifies the speed of the compressional wave, given by

$$V_p = \sqrt{\frac{\lambda + 2\mu}{\rho}}. \tag{23}$$

These equations are very similar to the asymptotic expressions for $\mathbf{x}$ and $\mathbf{p}$ along a ray path (Chapman 2004). Again, the presence of the wave potential in equation (22) couples that trajectory and slowness vector to the wave field amplitude. The requirement that $\mathbf{R}(\mathbf{x},\omega)$ have the form (20) is more restrictive and limits the modes of propagation, for example not allowing for mode conversions at boundaries that can occur if the equations (18) and (19) are used. However, due to the inclusion of the wave potential, the range of validity is still significantly greater then it is for high-frequency asymptotic ray theory.

Shear modes are associated with particle motion transverse to the direction of propagation. Such phases are important for imaging partial melts and the loss or rigidity. In an isotropic medium it is possible to study waves that have maintained their identity as shear waves throughout their propagation. Rectilinear shear motion in the plane transverse to $\mathbf{p}$ is given by

$$\mathbf{R}(\mathbf{x},\omega) = R(\mathbf{x},\omega)\mathbf{l}(\mathbf{x},\omega) \times \hat{\mathbf{p}}(\mathbf{x},\omega), \tag{24}$$

where $\mathbf{l}$ is a unit vector perpendicular to the motion. It we substitute the normalized form of this vector for $\hat{\mathbf{R}}$ in equations (18) and (19) then the terms containing $\mathbf{p} \cdot \hat{\mathbf{R}}$ vanish because the two vectors are perpendicular. As a result equations (18) and (19) become

$$\frac{d\mathbf{x}}{ds} = 2{V_s}^2\mathbf{p} \tag{25}$$

$$\frac{d\mathbf{p}}{ds} = -p^2\nabla_{\mathbf{x}}{V_s}^2 + \nabla_{\mathbf{x}}W, \tag{26}$$

where $V_s = \beta$ is the shear velocity given by equation (13).

2.3 Imaginary terms and the transport equation

2.3.1 General considerations

Due to the presence of the wave potential $W(\mathbf{x}, \omega)$ and other terms containing the amplitude vector $\mathbf{R}(\mathbf{x}, \omega)$, equations (18) and (19) are incomplete. As shown in the Appendix, equation (A14) provides a closed system of differential equations. This equation is obtained by considering the imaginary terms that result upon substituting the representation (3) into the elasto-dynamic equation of motion (2) and the equation that they define:

$$\nabla(\lambda\mathbf{k}\cdot\mathbf{R}) + \lambda\nabla\cdot\mathbf{Rk} + \nabla\mu\cdot\mathbf{Rk} + \nabla\mu\cdot\mathbf{kR} + \mu\nabla\mathbf{R}\cdot\mathbf{k}$$

$$+\mu\left(\nabla\mathbf{R}\right)^t\cdot\mathbf{k} + \mu\nabla\cdot(\mathbf{Rk}) + \mu\nabla\cdot(\mathbf{kR}) = 0. \tag{27}$$

Equation (27) is generally valid and makes no assumptions about the nature of the propagating wave front, other then that provided by the polar form (3). Therefore, the most general analysis would start from this equation. That is, equations (4) and (27) define a coupled system that describes the evolution of the phase φ and amplitude vector $\mathbf{R}$ of a propagating elastic wave. Both equations are non-linear partial differential equations and therefore difficult to solve. The non-linearity is to be expected, simply from the fact that the interaction of a single mode of propagation, such as a compressional wave, with a sharp boundary can lead to additional modes such as reflected and transmitted shear modes. As indicated above, the partial differential equation (4) is equivalent to the system of ordinary differential equations (18) and (19) for the trajectory $\mathbf{x}(s)$ and the slowness vector $\mathbf{p}$.

2.3.2 The transport equation for a compressional mode

In the remainder of this section we will focus on the study of compressional waves and will restrict our attention to those particular modes comprising the first arriving energy in a wave train. This involves an additional degree of approximation, as discussed in section 2.2. That is, we assume that the mode of propagation can be characterized along the propagation path, in this case as a compressional wave with displacement in the direction of $\mathbf{p}$.

We begin by projecting onto the direction of motion, that is, taking the scalar product of the terms in equation (27) and $\mathbf{R}$. $\mathbf{R}$ and $\mathbf{k}$ are parallel for the first arriving longitudinal wave, we can use the symmetry of the scalar products to collect similar terms and write equation (27) as

$$\nabla \cdot (\lambda \mathbf{k} \cdot \mathbf{RR}) + 2\nabla\mu \cdot \mathbf{Rk} \cdot \mathbf{R} \qquad (28)$$
$$+2\mu\mathbf{R} \cdot \nabla\mathbf{R} \cdot \mathbf{k} + 2\mu\mathbf{R} \cdot \nabla (\mathbf{k} \cdot \mathbf{R}) = 0.$$

Noting that the terms containing μ are just those that appear when we take the divergence of the vector quantity $2\mu\mathbf{k} \cdot \mathbf{RR}$, we can write equation (28) as a divergence

$$\nabla \cdot [(\lambda + 2\mu)\, \mathbf{k} \cdot \mathbf{RR}] = 0. \qquad (29)$$

If we divide both sides by ω, and account for the definition (7), we can write equation (29) in terms of $\mathbf{p}$

$$\nabla \cdot [(\lambda + 2\mu)\, \mathbf{p} \cdot \mathbf{RR}] = 0. \qquad (30)$$

Multiplying by ω^2 we can write this expression in terms of the velocity vector in the frequency domain $\mathbf{V}(\mathbf{x}, \omega)$

$$\nabla \cdot \left[\rho\alpha^2 \mathbf{p} \cdot \mathbf{VV}\right] = 0, \qquad (31)$$

where

$$\mathbf{V} = \omega\mathbf{R}, \qquad (32)$$

and we have used the definition (12) of $\alpha(\mathbf{x})$. We can write equation (31) as the divergence of the vector

$$\mathbf{N} = \rho\alpha^2 \mathbf{p} \cdot \mathbf{VV}, \qquad (33)$$

known as the energy flux vector, the equivalent of the Poynting vector in electromagnetism (Chapman 2004, p. 147). Equation (31) can be formulated as an ordinary differential equation if we apply the divergence operator to the product, giving

$$\mathbf{V} \cdot \nabla \left(\rho\alpha^2 \mathbf{p} \cdot \mathbf{V}\right) = -\rho\alpha^2 \mathbf{p} \cdot \mathbf{V} \nabla \cdot \mathbf{V}, \qquad (34)$$

and using the fact that $\mathbf{V} \cdot \nabla = d/dT$, where T is the travel time along the trajectory,

$$\frac{d}{dT} \ln \left(\rho\alpha^2 \mathbf{p} \cdot \mathbf{V}\right) = -\nabla \cdot \mathbf{V}, \qquad (35)$$

a variation of the transport equation. From the definition (32) we can substitute $\omega\mathbf{R}$ for $\mathbf{V}$ in equation (35) to produce an equation in terms of the displacement amplitude vector

$$\frac{d}{dT} \ln \left(\omega\rho\alpha^2 \mathbf{p} \cdot \mathbf{R}\right) = -\omega\nabla \cdot \mathbf{R}. \qquad (36)$$

This is a single equation in terms of $\mathbf{p}$ and $\mathbf{R}$ but we can rewrite it in terms of the amplitude of a longitudinal wave propagating along the trajectory $\mathbf{x}(s)$. That is, if we represent the amplitude vector by $\mathbf{R} = R\hat{\mathbf{p}}$, where R is the amplitude of the longitudinal wave, then equation (36) is a scalar ordinary differential equation in p and R.

2.4 Solutions of the elasto-dynamic equation of motion and the determination of the trajectory

Given an elastic model, along with initial and/or boundary conditions, we could solve the two sets of equations (8) and (27) for $\mathbf{k}$, and $\mathbf{R}$. Such a solution would provide the quantities necessary to construct a solution to the elasto-dynamic equation of motion (2). As a hypothetical example, consider a compressional wave impinging on a rapidly-varying velocity structure that resembles a step in properties, as in the examples given below. The solution of the two governing equations would provide the set of slowness vectors $\mathbf{k}$ and amplitudes $\mathbf{R}$ that result from the interaction of the impinging wavefield and the rapid variation in elastic properties. For a discontinuous step function with uniform values on either side of the boundary, such a calculation can be accomplished using other methods (Aki and Rickards 1980).

If we are only interested in the transmitted compressional wavefield, we could simplify the problem and focus on that mode of propagation, solving equations (21), (22), and (36). Similar considerations also apply to the transmitted shear mode. In order to determine the dependent variables, including the path $\mathbf{x}(s)$, we may apply numerical techniques for solving systems of ordinary differential equations, such as the Runge-Kutta method (Cash and Carp 1990, Press et al. 1992, Ascher and Petzold 1998). An additional complication arises due to the coupling between the amplitude and phase, as a result of the presence of the term $\nabla_{\mathbf{x}} W$ in equation (22). The trajectory now depends upon the spatial gradient of properties of the amplitude field, linking the calculations associated with adjacent trajectories. In spite of this, it is still possible to devise an efficient algorithm for constructing a trajectory-based solution, as is evident in applications to quantum dynamics (Wyatt 2005, Bittner et al. 2010, Garashchuk et al. 2011, Gu and Garashchuk 2016). These techniques have proven useful in modeling higher dimensional chemical systems and quantum mechanical effects in crystals (Wyatt 2005, Benseny et al. 2014). An alternative is to solve the coupled partial differential equations (11) and (30) using numerical techniques. Unfortunately, due to the coupling it is not possble to adopt a fast marching technique (Sethian 1999, Osher and Fedkiw 2003) directly, and the use of such methods will be the topic of future research.

As our interest is in the definition of the trajectories and in their use for visualization and imaging, we advance an alternative approach that is convenient if codes for waveform modeling are available. Specifically, we utilize a numerical code for the calculation of the wavefield and post-process the results to obtain the travel time field $T_{num}(\mathbf{x}, \omega)$. The slowness vector is the gradient of the travel time field, $\mathbf{p}_{num} = \nabla T_{num}$, and the trajectory is given by

$$\frac{d\mathbf{x}}{dT} = 2{V_p}^2 \mathbf{p}_{num}. \tag{37}$$

Given the slowness vector, equation (37) may be integrated numerically using a technique such as Huen's method, or a Runge-Kutta method (Cash and Carp 1990, Ascher and Petzold 1998). The technique is stable when marching down the gradient of the travel time field from a station location to the source point. The post-processing method should mirror the technique used to extract arrival times from the actual data. For example, one could use the same thresholding technique to determine the arrival times in both the observed and calculated wavefields. Travel times corresponding to specific frequencies can be estimated by filtering.

3 APPLICATIONS

We will illustrate the calculation of the extended trajectories using several velocity models. Interfaces and layers are considered first, as these are the most common features that are sharp and not smoothly-varying. A three-dimensional model for the Geysers geothermal area is explored next as an example of a velocity structure based upon a large set of geological, geophysical, and hydrological data (Hartline et al. 2015). Finally, we consider a travel time tomography application and indicate how the technique may be used to image fluid flow-related changes in seismic velocity. Our primary goal in this section is to compare the extended trajectories with ray paths computed using a conventional approach based upon the eikonal equation.

3.1 Trajectories in the presence of boundaries and layers

Layering is ubiquitous within the Earth and occurs over a wide variety of length scales. This fact presents a challange to methods that assume smoothly-varying properties in relation to the wave lengths of propagating elastic waves. In order to observe the break-down of the high-frequency approximation we will consider interfaces and layers with boundaries of variable sharpness. In particular, each interface will be represented as a transition zone from a region with one velocity to a region with a different velocity. The transition zone will be described mathematically by the function

$$f(z) = 1 - \frac{1}{2} \arctan \left[\sigma \left(z - z_i \right) \right] \quad (38)$$

where σ is a parameter signifying the abruptness of the boundary, larger values of σ correspond to sharper interfaces. The position of the interface is specified by the parameter z_i. Layers will be described by two such transition zones in close proximity.

3.1.1 Boundaries

The simplest boundary is an abrupt change in properties, as observed at various depths in the Earth such as the mantle discontinuities, the core-mantle boundary, and the inner core-outer core boundary. The exact transitional characteristics of these internal boundaries are still the topics of active research. Using equation (38), we consider three different transitions in properties across the boundary, as characterized by values of σ equal to 0.1, 1.0, and 10.0 (Figure 1). As is evident in Figure 1, $\sigma = 0.1$ produces a smoothly-varying transition zone for elastic waves with wavelengths of the order of hundreds of meters to a kilometer. We constructed a three dimensional model containing such a transition zone at a depth of 2 km, with a lateral extent of 5 km on a side. A vertical cross-section through the velocity model is plotted in Figure 2.

First, we calculate the ray paths, invoking the conventional high-frequency approximation leading to the eikonal equation (Aki and Richards 1980, Chapman 2004). The numerical solution of the eikonal equation described by Zelt and Barton (1998), a modification of the finite difference approach of Vidale (1988), is used to calculate the travel time field $T_{eikonal}(\mathbf{x})$. The ray paths are determined by solving the ordinary differential equation

$$\frac{d\mathbf{x}}{ds} = \nabla T_{eikonal} \quad (39)$$

using a Runge-Kutta based algorithm (Cash and Carp 1990). In essence, the algorithm simply marches down the gradient of the travel time field from the point of interest to the source location. The travel time field $T_{eikonal}(\mathbf{x})$ and the corresponding trajectories are plotted in Figure 2 for the model with the smooth transition.

The extended trajectories, are found by solving equation (37), which may be written as

$$\frac{d\mathbf{x}}{dT} = 2{V_p}^2 \nabla T_{num} \quad (40)$$

where $T_{num}(\mathbf{x}, \omega)$ is the travel time field obtained from a numerical solution of the elastic equations of motion. In the case shown in Figure 2 we use the finite-difference solution of the poroelastic equations described in Masson and Pride (2011) specialized to case in which the poroelastic effects are negligible. The source function is a Gaussian modulated by a sinusoidal function that varies as the frequency ω. In most of the examples in this sub-section, the central frequency ω is 3 Hz. For this model, with smoothly-varying properties, the trajectories based upon the eikonal equation and those resulting from solving equation (40) are essentially identical (Figure 2).

Equation (38) produces a much sharper transition zone when $\sigma = 10.0$, with a width of 0.1 km or less (Figures 1 and 3). In this case the trajectories based upon the eikonal equation may be divided into two groups, those that propagate down into the high velocity half-space and those that are not influenced by the high velocity region. The latter ray paths form straight line segments from the source to the receivers. In the middle panel in Figure 3 we observe a kink in the travel time field produced by the eikonal equation, separating the regions where these two groups of rays are important. For the high frequency traveltimes there are two evident kinks, one above the transition zone and one along it. Ray paths for receivers between the two kinks bend strongly into the half-space and propagate along the narrow transition zone. Rays outside of this region largely propagate along straight lines insensitive to the presence of the interface, except for the rays which cross it. The crossing rays bend at the interface approximating Snell's law of refraction from geometrical ray theory (Chapman 2004). In contrast, the travel times from the elastic wave equation are continuous and do not displays the sharp kinks produced by the eikonal equation (Figure 3). Correspondingly, the raypaths all appear to curve in response to the interface. None of the paths concentrate at the boundary, rather they dive under the transition zone and curve broadly within the high velocity half-space. Two paths deviate strongly from the high frequency asymptotic trajectories, those associated with the fourth and fifth receivers from the upper boundary.

From equations (14) and (22) one would expect that the conventional ray equations would become more accurate with increasing frequency. That is, because the wave potential $\hat{W}(\mathbf{x}, \omega)$ varies as $1/\omega^2$ the term should be 100 times smaller as ω varies from 1 to 10. In order to test this we consider source pulses with center frequencies of 1, 3, and 10 Hz, as shown in Figure 4. The medium corresponds to the half-space model with σ =1.0 shown in Figure 1. Vertical snapshots of the wavefields are also plotted in Figure 4 and they indicate that the wavelengths vary from around 2.0 km at 1.0 Hz to about 0.20 km at 10.0 Hz. The exact wavelength of the elastic disturbance depends upon the compressional velocity, which varies as a function of position within the medium. The resulting sets of trajectories for the three frequencies are shown in Figure 5. As ones progresses from the lowest frequency (1 Hz) to the highest (10 Hz) the trajectories within the lower, higher velocity, half-space become increasing concentrated at the boundary.

3.1.2 Layering

Layering, probably the most common form of heterogeneity within the Earth, may be considered to be the superposition of two interfaces. In addition to the width of the transition zone defining the edges of the layer, we also have the length scale associated with the thickness of the layer. In Figure 6 we plot three vertical velocity profiles associated with a layer approximately 100 m thick. The smoothness of the transition zones defining the edges of the layer are characterized by the function (38). For σ =0.1 the layer is quite smooth, while values of 0.5 and 10.0 produce rather abrupt boundaries and thin layers relative to wavelengths of the order of a few hundred meters or more. As in the previous sub-section we consider a source-time function with a dominant frequency of 3.0 Hz, as shown in Figure 4.

For a layer with edges defined by equation (38) with $\sigma = 0.1$, the eikonal and extended trajectories are very similar, as shown in Figure 7. Increasing σ to 0.5 results in a layer with moderately sharp boundaries (Figures 6 and 8). The rays based upon the eikonal equation either propagate above the layer unaffected by the nearby velocity variation, or propagate steeply down into the layer and then spread out to the various receivers at the rightmost edge of the model (Figure 8). The influence of the layer is more wide-spread in the trajectory mechanics approach and most of the paths above the layer bend in response to its higher velocities. Several of the trajectories are significantly different from those of the eikonal equation, in particular those starting from the fourth and fifth receivers. As in the case of the half-spaces, the travel time field associated with the eikonal equation displays a kink that is not observed in the travel time field from the numerical simulator.

3.2 An example velocity model from The Geysers

As an example of a more complicated model, we consider a three-dimensional velocity structure for a selected area of the Geysers geothermal area in California. The velocity variation is based upon a structural model constructed from approximately 870 lithology logs, surface geology maps, reservoir temperature and pressure observations, tracer tests and reservoir history matching, and microseismic data (Hartline et al. 2015). The structural model consists of surfaces separating major lithologies such as graywacke/argillite, greenstone, serpentinite, melange, and felsite (Figure 9). Given the lithologic boundaries from well information, it was necessary to populate the model with seismic velocities. Due to the harsh reservoir conditions, including high temperatures and corrosive fluids, conventional geophysical logging methods developed for oil and gas applications are not practical at the Geysers (Hartline et al. 2015). As a result of these complications, there are few direct measurements of elastic properties from wells at the Geysers and seismic tomography remains the most common approach for obtaining information on compressional and shear velocities (Julian et al. 1996, Gritto et al. 2013, Gritto and Jarpe 2014). We used the velocity model of Gritto et al. (2013) to populate our structural model with seismic velocities. The model is 5 km by 5 km in the east-west and north-south directions and 5 km in depth. An east-west cross-section through the velocity model, intersecting our source location, is shown in Figure 10. The structure consists of constant velocity layers separated by velocity gradients, capturing the large-scale spatial variations in seismic properties. The ground surface is indicated by a large change in seismic velocity at a depth of around 0.9 km.

In order to compare the trajectories calculated using the eikonal equation with those from the trajectory mechanics approach, we considered a source at (x, y, z) =(1.0 km, 2.5 km, 2.725 km), indicated by the unfilled star in Figure 10. Equations (39) and (40) were used to find the eikonal and extended ray paths from the source to nine receivers near the surface and several points at the eastern edge of the model (Figure 10). The travel time field $T_{eikonal}$ is computed using the numerical routines of Zelt and Barton (1998). The dominant frequency of the source used in the finite difference calculations to determine $T_{num}(\mathbf{x}, \omega)$ was 1.0 Hz. While many of the trajectories are similar for the two methods, there are significant differences of 100 m or so for several paths to points at the right edge of the model. Paths calculated using the eikonal equation concentrate in the high velocity zone near the base of the model. The largest deviations are just above this higher velocity layer, similar to the differences observed in Figures 3 and 8. Note that this is only a representation of the large-scale velocity variations at the Geysers. That is, we can expect highly heterogeneous smaller scale structure to be superimposed on the velocity variations in Figure 10. Correspondingly, the eikonal-based ray paths and those from the trajectory mechanics approach should display even greater differences if such variations are included in a detailed velocity model.

3.3 Tomographic Imaging

The extended trajectories can be used for tomographic imaging of velocity heterogeneity using seismic arrival times. Here we will consider travel times associated with first arriving compressional waves and the corresponding equations (21) and (22). In order to calculate model parameter sensitivities one can utilize equation (21) and integrate along the trajectory to derive an expression for the travel time

$$T = \int_{\mathbf{x}} \frac{ds}{2{V_p}^2|\mathbf{p}|}. \tag{41}$$

We can apply a perturbation method to the expression (41), or the Born approximation (Coates and Chapman 1990), to estimate model parameter sensitivities for the inverse problem. Note that, if the eikonal equation was valid we could use it to cancel $|\mathbf{p}|$ and a factor of V_p in equation (41), leading to the conventional expression relating T and V_p along the trajectory. For small perturbations in $V_p(\mathbf{x})$ we shall assume that the changes in the trajectories and the slowness vector are second order and that we can use values from calculations made using the background model, perhaps the last iteration of a linearized inversion algorithm. Furthermore, we consider the slownesses,

$$S_p(\mathbf{x}) = \frac{1}{V_p(\mathbf{x})} \tag{42}$$

the inverse of the velocities, as the primary unknowns. Perturbing the slowness model

$$S_p(\mathbf{x}) = S_o(\mathbf{x}) + \delta S(\mathbf{x}), \tag{43}$$

where $S_o(\mathbf{x})$ is the slowness of the background model, and neglecting changes in the background quantities gives an expression for the perturbation of the arrival time in terms of an integral of the slowness perturbations along the trajectory

$$\delta T = \int_{\mathbf{x}_o} \frac{S_o}{|\mathbf{p}_o|} \delta S ds, \tag{44}$$

which differs from that used in current tomographic imaging approaches due to the presence of the factor $S_o/|\mathbf{p}_o|$.

We have implemented this approach for tomographic imaging, tested it on synthetic arrival times, and applied it to travel time data from a crosswell imaging experiment. The arrival times were gathered during the monitoring of a fracturing and remediation experiment at the Warren Air Force Base near Cheyenne, Wyoming (Ajo-Franklin et al. 2011). The multi-level continuous active source seismic monitoring system (ML-CASSM) was used to gather complete crosswell surveys every 3 to 4 minutes. As described in Ajo-Franklin et al (2011) fluid was injected into a horizontal fracture that intersected the plane defined by the two wells. In order to image the velocity changes associated with the appearance of the fluid within the fracture, we adopted an iterative approach in which we conducted numerical simulations of the wavefields propagating from the nine sources to the receivers in order to estimate the travel time field T_{num} and $\mathbf{p}_{num} = \nabla T_{num}$. Thus, we defined the quantities in equation (44) and calculated the trajectories $\mathbf{x}_o$ from the sources to the receivers. Two sets of trajectories from the 3rd and 8th sources are plotted in Figure 11. The ray coverage provided by all nine sources to the active receivers is also plotted in this figure for the final iteration. The velocity variations determined by inverting the arrival times are shown in Figure 12. A low velocity feature, at the estimated depth of the fracture, is observed. The feature is somewhat sharper than the results of previous work using a conventional approach based upon the eikonal equation (Ajo-Franklin et al. 2011). Also, the anomally in Figure 12 is offset from the receiver well, in accordance with expectations, while conventional imaging put the largest values at the receiver well. Synthetic testing indicated that conventional eikonal equation-based imaging can lead to preferential anomalies near the sources and receivers for narrow low velocity features.

4 DISCUSSION

Most tomographic imaging algorithms rely on a high frequency approximation and the eikonal equation for calculating ray paths and sensitivities for the inverse problem. The limitations of such a high-frequency approach have been well documented in the literature (Wielandt 1987, Woodward 1992, Stark and Nikolayev 1993). Alternative methods for the interpretation of travel times, such as a technique based upon the cross-correlation of observed and calculated pulses (Luo and Schuster 1991, Luo 1991, Vasco and Majer 1993, Marquering et al. 1999), have been developed. While such approaches do account for the frequency content of the pulse through the use of waveform calculations, the majority of first arrival times are not obtained by cross-correlation but rather from picking the first break of an arriving pulse. It is not clear that the sensitivities of a first break are equivalent to those of a cross-correlation time because, as shown in Keers et al. (2000), the early time sensitivities of a pulse differ from those associated with the peak of the pulse. For example, the peak sensitivity for a point just after the onset of the pulse is along the geometrical ray, while the sensitivity for a point near the peak is largest not on the ray but adjacent to the geometrical path (Marquering et al. 1999). Furthermore, in the presence of significant lateral heterogeneity it can be difficult to establish an initial model that is sufficient to initiate the necessary waveform calculations for the cross-correlation approach (Zelt and Chen 2016). For an imaging approach based upon the broad band trajectories we do not have to use cross-correlation arrival times. Rather, one can simply apply the same approach to estimating the first arrival times from the recorded seismic data to calculate arrival times from the numerical simulation results.

5 CONCLUSIONS

Using methods originally developed in quantum mechanics (Wyatt 2005) and recently applied in hydrodynamics (Vasco 2018, Vasco et al. 2018), we have derived a trajectory-based solution to the elasto-dynamic equation of motion that is valid for rapid spatial variations in elastic properties. The idea is similar in philosophy to Helmholtz tomography (Lin and Ritzwoller 2011, Kohler et al. 2018) where amplitude gradients are used to correct phase measurements using the Helmholtz equation. Here, we derive complete expressions for the trajectory, slowness, and amplitude of a propagating elastic disturbance directly from the elasto-dynamic equation of motion. Coupling this approach with a numerical routine for solving the governing equation, such as one based upon finite differences (Virieux 1986, Petrov and Newman 2012) or spectral-elements (Komatitsch et al. 2002), allows for the calculation of trajectories by simply post-processing the results of a simulation.

As expected, the broad band trajectories agree with conventional high-frequency asymptotic ray paths for velocity models that display smoothly-varying heterogeneity. However, the high-frequency paths and the extended trajectories begin to deviate when rapid spatial variations are introduced into the velocity model, particularly for those rays that pass close to interfaces or layer boundaries. The differences are particularly pronounced for a layered model when the layer thickness is less then the dominant wavelength. The deviations depend upon the frequency of the propagating waves, and the extended trajectories do approach the high frequency solutions as ω becomes large. Calculations for a velocity model based upon field data also indicates that substantial differences are possible for local wave propagation at frequencies of around 1 Hz. The exact criterion for the significance of the wave potential follows from the Hamiltonian given by the expression (16). In particular, when the magnitude of the wave potential $W(\mathbf{x}, \omega)$ approaches 1, that is when

$$W(\mathbf{x}, \omega) = \frac{1}{\rho R \omega^2} \mathbf{F} \cdot \hat{\mathbf{R}} \sim 1, \tag{45}$$

then the coupling between the phase and amplitude becomes an important factor. One can use a similarity argument or dimensional analysis to normalize the variables, for example scaling the spatial coordinates $\mathbf{x}$ by the wavelength of the disturbance L. Using such arguments one can deduce that the coupling is important when

$$\frac{\nabla \lambda + \nabla \mu}{L} \sim \rho \omega^2, \tag{46}$$

suggesting that the wave potential can be important at any scale if the elastic properties vary rapidly enough.

The trajectories can serve as the basis for a semi-analytic travel time tomographic imaging algorithm with an extended range of validity. This can be helpful due to the many advantages associated with travel time tomography. For example, the inverse problem associated with the use of seismic arrival times is quasi-linear and its convergence is less sensitive to the initial or starting velocity model. Therefore, travel time tomography is often used to find an initial model prior to waveform inversion. Travel times extracted from seismic waveforms reduce the data handling burden that is characteristic of waveform imaging. Furthermore, the use of waveforms is complicated by the sensitivity of amplitudes to many factors, such as source-receiver coupling, source and receiver orientation, receiver calibration, and variations in source power.

ACKNOWLEDGMENTS

This material is based upon work supported by the U.S. Department of Energy, Office of Science, Office of Basic Energy Sciences, Chemical Sciences, Geosciences, and Biosciences Division under contract number DE-AC02-05- CH11231. We would like to thank Y. Masson for the use of his finite difference code for modeling wave propagation in a poroelastic medium.

REFERENCES

Ajo-Franklin, J., Daley, T., Butler-Veytia, B., Peterson, J., Wu, Y., Kelly, B., and Hubbard, S., 2011, Multi-level continuous active source seismic monitoring (ML-CASSM): Mapping shallow hydrofracture evolution at a TCE contaminated site, *Society of Exploration Geophysics Expanded Abstracts*, **30**, 3727 (2011), doi: 10.1190/1.3627980.

Aki, K., and Lee, W. K. H. (1976). Determination of three-dimensional velocity anomalies under a seismic array using first P arrivaltimes from local earthquakes: 1. A homogeneous initial model, *Journal of Geophysical Research*, **81**, 4381-4399.

Aki, K., Christoffersson, A., and Husebye E. S. (1976). Determination of the three-dimensional seismic structure of the lithosphere, *Journal of Geophysical Research*, **82**, 277-296.

Aki, K., and Richards, P. G., 1980. *Quantitative Seismology*, Freeman and Sons, San Francisco.

Alkhalifah, T., and Choi, Y. (2012). Taming waveform inversion non-linearity through phase unwrapping of the model and objective functions, *Geophysical Journal International*, **191**, 1171-1178.

Ascher, U. M., and L. R. Petzold (1998). *Computer Methods for Ordinary Differential Equations and Differential-Algebraic Equations*, Society for Industrial and Applied Mathematics, Philadelphia.

Aster, R. C., Borchers, B., and Thurber, C. H., 2013. *Parameter Estimation and Inverse Problems*, Elsevier, Waltham, MA.

Ben-Menahem, A., and Singh, S. J. (1981). *Seismic Waves and Sources*, Springer-Verlag, New York.

Bharadwaj, P., Mulder, W., and Drijkoningen, G. (2016). Full waveform inversion with an auxiliary bump functional, *Geophysical Journal International*, **206**, 1076-1092, https://doi.org/10.1093/gji/ggw129.

Benseny, A., Albareda, G., Sanz, A. S., Mompart, J., and Oriols, X., 2014. Applied Bohmian mechanics, *European Physics Journal*, **68**, 286.

Bijwaard, H. and Spakman (2000). Non-linear global P-wave tomography by iterated linearized inversion, *Geophysical Journal International*, **141**, 71-82.

Bittner, E. R., Kouri, D. J., Derrickson, S., and Maddox, J. B. (2010). Variational Quantum Hydrodynamics, in *Applied Bohmian Dynamics: From Nanoscale Systems to Cosmology*, X. Oriols, and J. Mompart (eds.), Pan Stanford Publishing, Singapore.

Cash, J. R., and A. H. Carp (1990). A variable order Runge-Kutta method for initial value problems with rapidly varying right-hand sides, *ACM Transactions on Mathematical Software*, **16**, 201-222.

Chapman, C. H. (2004). *Fundamentals of Seismic Wave Propagation*, Cambridge University Press, Cambridge.

Coates, R. T., and Chapman, C. H. (1990). Ray perturbation theory and the Born approximation, *Geophysical Journal International*, **100**, 379-392.

Courant, R., and Hilbert, D. (1962). *Methods of Mathematical Physics*, John Wiley and Sons, New York.

Dessa, J.-X. and Pascal, G. (2003). Combined traveltime and frequency-domain seismic waveform inversion: a case study on multi-offset ultrasonic data, *Geophysical Journal International*, **154**, 117-133.

Dines, K. A., and Lytle, R. J. (1979). Computerized geophysical tomography, *Proceedings of the IEEE*, **67**, 1065-1073.

Dziewonski, A. M., Hager, B. H., and O'Connell, R. J. (1977). Large-scale heterogeneities in the lower mantle, *Journal of Geophysical Research*, **82**, 239-255.

Garashchuk, S., J. Mazzuca, and T. Vazhappilly (2011). Efficient quantum trajectory representation of wavefunctions evolving in imaginary time, *Journal of Chemical Physics*, **135**, 034104, doi: 10.1063/1.3610165.

Gritto, R., and Jarpe, S. P. (2014). Temporal variations of V_p/V_s-ratio at The Geysers geothermal field, USA, *Geothermics*, **52**, 112-119., http://dx.doi.org/10.1016/j.geothermics.2014.01.012.

Gritto, R., Yoo, S.-H., and Jarpe, S. P. (2013). Three-dimensional seismic tomography at the Geysers geothermal field, CA, USA, *38th Workshop on Geothermal Reservoir Engineering*, SGP-TR-198, 1-12, Stanford University, Stanford, California, February 11-13, 2013.

Gu, B., and Garashchuk, S. (2016). Quantum dynamics with Gaussian bases defined by quantum trajectories, *Journal of Physical Chemistry*, **120**, 3023-3031, doi: 10.1021/acs.jpca.5b10029

Hager, B. H., and Clayton, R. W. (1989). Constraints on the structure of the mantle using seismic observations, flow models, and the geoid, in *Mantle Convection*, Peltier, W. R. (ed.), Gordon and Breach, New York.

Hartline, C. S., Walters, M. A., and Wright, M. C. (2015). Three-dimensional structural model building, induced seismicity analysis, drilling analysis, and reservoir management at the Geysers geothermal field, northern California, *GRC Transactions*, **39**, 603-614.

Holliger, K. (1996). Upper crustal seismic velocity heterogeneity as derived from a variety of P-wave sonic logs, *Geophysical Journal International*, **125**, 813-829.

Inoue, H., Fukao, Y, Tanabe, K., and Ogata, Y. (1990). Whole mantle P-wave travel time tomography, *Physics of Earth and Planetary Interiors*, **59**, 294-328.

Iyer, H. M., and Hirahara, K. (1993). *Seismic Tomography*, Chapman and Hall, London.

Julian, B. R., Ross, A., Foulger, G. R., and Evans, J. R. (1996). Three-dimensional seismic image of a geothermal reservoir: The Geysers, California *Geophysical Research Letters*, **23**, doi:10.1029/96GL03321.

Karal, C. F. and Keller, J. B. (1959). Elastic wave propagation in homogeneous and inhomogeneous media, *Journal of the Acoustical Society of America*, **31**, 694-705.

Keers, H., Johnson, L., and Vasco, D. (2000). Acoustic crosswell imaging using asymptotic waveforms, *Geophysics*, **65**, 1569-1582.

Kline, M. and Kay, I. W. (1965). *Electromagnetics Theory and Geometrical Optics*, Interscience Publishers, New York.

Kohler, M. D., Allam, A., Massari, A., and Lin, F.-C. (2018). Detection of building damage using

Helmholtz tomography, *Bulletin of the Seismological Society of America*, **78**, 2062-2076.

Komatitsch, D., Ritsema, J., and Tromp, J. (2002). The spectral-element method, Beowulf computing, and global seismology, *Science*, **298**, 1737-1742, doi: 10.1126/science.1076024.

Leary, P. (1991). Deep borehole evidence for fractal distribution of fractures in crystalline rock, *Geophysical Journal International*, **107**, 615-627.

Lin, F.-C. and Ritzwoller, M. H.. (2011). Helmholtz surface wave tomography for isotropic and azimuthally anisotropic structure, *Geophysical Journal International*, **186**, 1104-1120.

Lomax, A. (1994). The wavelength-smoothing method for approximating broad-band propagation through complicated velocity structures, *Geophysical Journal International*, **117**, 313-334.

Lomax, A. and Snieder, R. (1996). Estimation of finite-frequency waveforms through wavelength-dependent averaging of velocity, *Geophysical Journal International*, **126**, 369-381.

Luneburg, R. K. (1996). *Mathematical Theory of Optics*, University of California Press, Berkeley.

Luo, Y., 1991. Calculation of Wavepaths for band-limited seismic waves, *61st Annual Meeting Soc. Explor. Geophys., Expanded Abstracts*, 1509-1512.

Luo, Y., and G. T., Schuster (1991). Wave-equation traveltime inversion, *Geophysics*, **56**, 645-653, doi.org/10.1190/1.1443081.

Marquering, H., Dahlen, F. A., and Nolet, G. (1999). Three-dimensional sensitivity kernels for finite-frequency traveltimes: the banana-doughnut paradox, *Geophysical Journal International*, **137**, 805-815.

Masson, Y. J., and Pride, S. R. (2011). Seismic attenuation due to patchy saturation, *Journal of Geophysical Research*, **116**, 1-17, doi:10.1029/2010JB007983.

McMechan, G. A. (1983). Seismic tomography in boreholes, *Geophysical Journal of the Royal Astronomical Society*, **74**, 601-612.

Osher, S., and R. Fedkiw (2003). *Level Set Methods and Dynamic Implicit Surfaces*, Springer, New York.

Peterson, J. E., Paulsson, B. N., and McEvilly, T. V. (1985). Applications of algebraic reconstruction techniques to crosshole seismic data, *Geophysics*, **50**, 1566-1580.

Petrov, P. V., and Newman, G. A. (2012). 3D finite-difference modeling of elastic wave propagation in the Laplace-Fourier domain, *Geophysics*, **77**, T137-T155, https://doi.org/10.1190/geo2011-0238.1.

Podvin, P., and I. Lecomte (1991). Finite-difference computation of traveltimes in very contrasted velocity models: A massively parallel approach and its associated tools, *Geophysical Journal International*, **105**, 271-284.

Press, W. H., S. A. Teukolsky, W. T. Vetterling, and B. P. Flannery (1992). *Numerical Recipes*, Cambridge University Press, Cambridge.

Pulliam, R. J., Vasco, D. W., and Johnson, L. R. (1993). Tomographic inversions for mantle P wave velocity structure based on minimization of l^2 and l^1 norms of International Seismological Centre travel time residuals, *Journal of Geophysical Research*, **98**, 699-734.

Rudnicki, J. W. (2015). *Fundamentals of Continuum Mechanics*, Wiley, Chichester.

Savran, W. H., and Olsen, K. B. (2016). Model for small-scale crustal heterogeneity in Los Angeles basin based on inversion of sonic log data, *Geophysical Journal International*, **205**, 856-863.

Sengupta, M. K., and Toksoz, M. N. (1976). Three-dimensional model of seismic velocity variation in the Earth's mantle, *Geophysical Research Letters*, **3**, 84-86.

Serretti, P. and Morelli, A. (2011). Seismic rays and traveltime tomography of strongly heterogeneous mantle structure: application to the Central Mediterranean, *Geophysical Journal International*, **187**, 1708-1724.

Sethian, J. A. (1999). *Level Set Methods and Fast Marching Methods*, Cambridge University Press, Cambridge.

Stark, P, and Nikolayev, D. I. (1993). Toward tubular tomography, *Journal of Geophysical Research*, **98**, 8095-8106.

Thurber, C. H. (1983). Earthquake locations and three-dimensional crustal structure in the Coyote Lake area, central California, *Journal of Geophysical Research*, **88**, 8226-8236.

Vasco, D. W. (2018). An extended trajectory mechanics approach for calculating the path of a pressure transient: Derivation and illustration, *Water Resources Research*, **54**, https://doi.org/10.1002/2017WR021360.

Vasco, D. W. and Datta-Gupta, A. (2016). *Subsurface Fluid Flow and Imaging*, Cambridge University Press, Cambridge.

Vasco, D. W., and E. L. Majer (1993). Wavepath traveltime tomography, *Geophysical Journal International*, **115**, 1055-1069, doi: 10.1111/j.1365-246X.1993.tb01509.x

Vasco, D. W., Pride, S. R., Zahasky, C., and Benson, S. M. (2018). Calculating trajectories associated with solute transport in a heterogeneous medium, *Water Resources Research*, **54**, https://doi.org/10.1029/2018WR023019.

Vasco, D. W., and Johnson, L. R., and Marques, O. (2003). Resolution, uncertainty, and whole Earth tomography, *Journal of Geophysical Research*, **108**, 1-26, doi:10.1029/2001/JB000412.

Vidale, J. (1988). Finite-difference calculation of traveltimes, *Bulletin of the Seismological Society of America*, **78**, 2062-2076.

Virieux, J. (1986). P-SV wave propagation in heterogeneous media: Velocity-stress finite-difference method, *Geophysics*, **51**, 889-901.

Wielandt, E. (1987). On the validity of the ray approximation for interpreting delay times in *Seismic Tomography with Applications in Global Seismology and Exploration Geophysics*, Nolet, G. (ed.), D. Reidel Publishing Co., Dordrecht Holland.

Woodward, M. J. (1992). Wave-equation tomography, *Geophysics*, **57**, 15-26.

Wyatt, R. E. (2005). *Quantum Dynamics with Trajectories*, Springer, New York.

Zelt, C. A., and Barton, P. J. (1998). 3D seismic refraction tomography: A comparison of two methods applied to data from the Faeroe Basin, *Journal of Geophysical Research*, **103**, 7187-7210.

Zelt, C. A., and Chen, J. (2016). Frequency-dependent traveltime tomography for near-surface seismic refraction data, *Geophysical Journal International*, **207**, 72-88, doi: 10.1093/gji/ggw269.

6 APPENDIX

In this Appendix we provide some of the steps required in order to derive equations (4) and (27) found in the main body of the paper. We will employ dyadic notation, in which the multiplication of vectors signify outer products (Ben-Menahem and Singh 1981, p. 1, Rudnicki 2015, p. 25, Vasco and Datta-Gupta 2016, p. 293). We begin with an expanded version of the governing equation (2)

$$-\rho\omega^2\mathbf{U} = \nabla\lambda\nabla\cdot\mathbf{U} + \lambda\nabla\left(\nabla\cdot\mathbf{U}\right) + \nabla\mu\cdot\left[\nabla\mathbf{U} + \left(\nabla\mathbf{U}\right)^t\right]$$

$$+\mu\nabla\cdot\nabla\mathbf{U} + \mu\nabla\cdot\left(\nabla\mathbf{U}\right)^t. \qquad (A1)$$

Substituting the representation

$$\mathbf{U}(\mathbf{x},\omega) = \mathbf{R}(\mathbf{x},\omega)e^{-i\varphi(\mathbf{x},\omega)} \qquad (A2)$$

into equation (A1) gives

$$-\rho\omega^2\mathbf{R}e^{-i\varphi} = \nabla\lambda\nabla\cdot\left(\mathbf{R}e^{-i\varphi}\right) + \lambda\nabla\nabla\cdot\left(\mathbf{R}e^{-i\varphi}\right)$$

$$+\nabla\mu\cdot\nabla\left(\mathbf{R}e^{-i\varphi}\right) + \nabla\mu\cdot\left[\nabla\left(\mathbf{R}e^{-i\varphi}\right)\right]^t \qquad (A3)$$

$$+\mu\nabla\cdot\nabla\left(\mathbf{R}e^{-i\varphi}\right) + \mu\nabla\cdot\left[\nabla\left(\mathbf{R}e^{-i\varphi}\right)\right]^t.$$

Applying the differential operators to the quantities in parentheses and factoring out the multiplier $e^{-i\varphi}$ that appears in all of the terms, results in an expression containing both real and imaginary components.

$$-\rho\omega^2\mathbf{R} = \nabla\lambda\nabla\cdot\mathbf{R} + i\nabla\lambda\mathbf{R}\cdot\nabla\varphi$$

$$+\lambda\nabla\left(\nabla\cdot\mathbf{R}\right) + i\lambda\nabla\cdot\mathbf{R}\nabla\varphi + i\lambda\nabla\left(\nabla\varphi\cdot\mathbf{R}\right) - \lambda\left(\nabla\varphi\cdot\mathbf{R}\right)\nabla\varphi$$

$$+\nabla\mu\cdot\nabla\mathbf{R} + i\nabla\mu\cdot\left(\mathbf{R}\nabla\varphi\right)$$

$$+\nabla\mu\cdot\left(\nabla\mathbf{R}\right)^t + i\nabla\mu\cdot\left(\nabla\varphi\mathbf{R}\right)$$

$$+\mu\nabla\cdot\nabla\mathbf{R} + i\mu\nabla\mathbf{R}\cdot\nabla\varphi + i\mu\nabla\cdot\mathbf{R}\nabla\varphi + i\mu\mathbf{R}\nabla\cdot\nabla\varphi - \mu\mathbf{R}\nabla\varphi\cdot\nabla\varphi$$

$$+\mu\nabla\cdot\left(\nabla\mathbf{R}\right)^t + i\mu\left(\nabla\mathbf{R}\right)^t\cdot\nabla\varphi + i\mu\nabla\cdot\nabla\varphi\mathbf{R} + i\mu\nabla\varphi\nabla\cdot\mathbf{R}$$

$$-\mu\nabla\varphi\mathbf{R}\cdot\nabla\varphi. \qquad (A4)$$

698 ### 6.1 Real Terms

If we consider only the real terms in equation (A4), and move the terms containing $\nabla\varphi$ to the left-hand-side, the resulting equation is

$$\lambda\left(\nabla\varphi\cdot\mathbf{R}\right)\nabla\varphi+\mu\mathbf{R}\nabla\varphi\cdot\nabla\varphi+\mu\nabla\varphi\mathbf{R}\cdot\nabla\varphi$$

$$=\rho\omega^2\mathbf{R}+\nabla\lambda\nabla\cdot\mathbf{R}+\lambda\nabla\left(\nabla\cdot\mathbf{R}\right)+\nabla\mu\cdot\nabla\mathbf{R}$$

$$+\nabla\mu\cdot\left(\nabla\mathbf{R}\right)^t+\mu\nabla\cdot\nabla\mathbf{R}+\mu\nabla\cdot\left(\nabla\mathbf{R}\right)^t. \qquad (A5)$$

Using the symmetry of the scalar product and collecting terms, we can write equation (A4) somewhat more succently as

$$\left(\lambda+\mu\right)\nabla\varphi\cdot\mathbf{R}\nabla\varphi+\mu\nabla\varphi\cdot\nabla\varphi\mathbf{R}-\rho\omega^2\mathbf{R}$$

$$=\left(\nabla\cdot\mathbf{R}\right)\nabla\lambda+\nabla\cdot\mu\left[\nabla\mathbf{R}+\left(\nabla\mathbf{R}\right)^t\right]. \qquad (A6)$$

The terms on the right-hand-side do not contain $\nabla\varphi$ and we can define a vector

$$\mathbf{F}(\mathbf{x},\omega)=\left(\nabla\cdot\mathbf{R}\right)\nabla\lambda+\nabla\cdot\mu\left[\nabla\mathbf{R}+\left(\nabla\mathbf{R}\right)^t\right] \qquad (A7)$$

and equation (A6) takes the form

$$\left(\lambda+\mu\right)\nabla\varphi\cdot\mathbf{R}\nabla\varphi+\mu\nabla\varphi\cdot\nabla\varphi\mathbf{R}-\rho\omega^2\mathbf{R}=\mathbf{F}(\mathbf{x},\omega).$$

$$(A8)$$

We can rewrite equation (A8) into a form that is somewhat similar to the eikonal equation if we define the wave number vector

$$\mathbf{k}=\nabla\varphi \qquad (A9)$$

and the related slowness vector

$$\mathbf{p}=\frac{\mathbf{k}}{\omega}. \qquad (A10)$$

If we divide equation (A8) by ω^2 and ρ, and make use of the definitions (A9) and (A10), then we may write it in terms of $\mathbf{p}$

$$\frac{(\lambda+\mu)}{\rho}\mathbf{p}\cdot\mathbf{R}\mathbf{p}+\frac{\mu}{\rho}\mathbf{p}\cdot\mathbf{p}\mathbf{R}-\mathbf{R}=\frac{1}{\rho\omega^2}\mathbf{F}(\mathbf{x},\omega). \qquad (A11)$$

When the frequency ω is high and the gradients of the wavefield amplitudes contained in $\mathbf{F}(\mathbf{x},\omega)$ are not too large, we may neglect the right-hand-side of equation (A11). The equation then begins to resemble the conventional eikonal equation but for the presence of the factors of $\mathbf{R}$ that prevent us from collapsing the first two terms into one containing $\mathbf{p}\cdot\mathbf{p}$. As noted in section 2.2, depending on the orientation of the amplitude $\mathbf{R}$ with respect to the slowness vector $\mathbf{p}$ equation (A11) can lead to a governing equation for compressional or shear modes of propagation.

6.2 Imaginary Terms

Now consider the imaginary terms in equation (A4), defining a second partial differential equation in φ and $\mathbf{R}$. If we set the sum of all of the imaginary terms to zero, we arrive at the vector differential equation

$$\nabla\lambda\mathbf{R}\cdot\nabla\varphi+\lambda\left(\nabla\cdot\mathbf{R}\right)\nabla\varphi+\lambda\nabla\left(\nabla\varphi\cdot\mathbf{R}\right)$$
$$+\nabla\mu\cdot\left(\mathbf{R}\nabla\varphi\right)+\nabla\mu\cdot\left(\nabla\varphi\mathbf{R}\right)+\mu\left[\nabla\mathbf{R}+\left(\nabla\mathbf{R}\right)^{t}\right]\cdot\nabla\varphi$$
$$+\mu\nabla\cdot\left(\mathbf{R}\nabla\varphi\right)+\mu\nabla\cdot\left(\nabla\varphi\mathbf{R}\right)=0. \qquad (A12)$$

Re-arranging the terms containing λ produces

$$\nabla\left(\lambda\mathbf{R}\cdot\nabla\varphi\right)+\lambda\nabla\cdot\mathbf{R}\nabla\varphi$$
$$+\nabla\mu\cdot\left(\mathbf{R}\nabla\varphi\right)+\nabla\mu\cdot\left(\nabla\varphi\mathbf{R}\right)+\mu\left[\nabla\mathbf{R}+\left(\nabla\mathbf{R}\right)^{t}\right]\cdot\nabla\varphi$$
$$+\mu\nabla\cdot\left(\mathbf{R}\nabla\varphi\right)+\mu\nabla\cdot\left(\nabla\varphi\mathbf{R}\right)=0. \qquad (A13)$$

At first glance, equations (A8) and (A13) are first and second order in φ respectively. However, φ only appears as $\mathbf{k}=\nabla\varphi$ in these equations. Thus, if we substitute for $\nabla\varphi$ in equation (A13)

$$\nabla\left(\lambda\mathbf{R}\cdot\mathbf{k}\right)+\lambda\nabla\cdot\mathbf{R}\mathbf{k}+\nabla\mu\cdot\mathbf{R}\mathbf{k}+\nabla\mu\cdot\mathbf{k}\mathbf{R}+\mu\nabla\mathbf{R}\cdot\mathbf{k}$$
$$+\mu\left(\nabla\mathbf{R}\right)^{t}\cdot\mathbf{k}+\mu\nabla\cdot\left(\mathbf{R}\mathbf{k}\right)+\mu\nabla\cdot\left(\mathbf{k}\mathbf{R}\right)=0. \qquad (A14)$$

Alternatively, using the fact that $\mathbf{k}=\omega\mathbf{p}$, we can diving equation (A14) by ω to write it as

$$\nabla\left(\lambda\mathbf{R}\cdot\mathbf{p}\right)+\lambda\nabla\cdot\mathbf{R}\mathbf{p}+\nabla\mu\cdot\mathbf{R}\mathbf{p}+\nabla\mu\cdot\mathbf{p}\mathbf{R}+\mu\nabla\mathbf{R}\cdot\mathbf{p}$$
$$+\mu\left(\nabla\mathbf{R}\right)^{t}\cdot\mathbf{p}+\mu\nabla\cdot\left(\mathbf{R}\mathbf{p}\right)+\mu\nabla\cdot\left(\mathbf{p}\mathbf{R}\right)=0. \qquad (A15)$$

The two vector equations (A8) and (A14) can be used to solve for $\mathbf{k}$ and $\mathbf{R}$. One could consider equation (A8) as having $\mathbf{k}$ as a multiplier, containing no derivatives of its components, and equation (A13) as first-order in the components. Equation (A8) is second-order in $\mathbf{R}$ while equation (A14) is first order in terms of the components of $\mathbf{R}$.

Figures

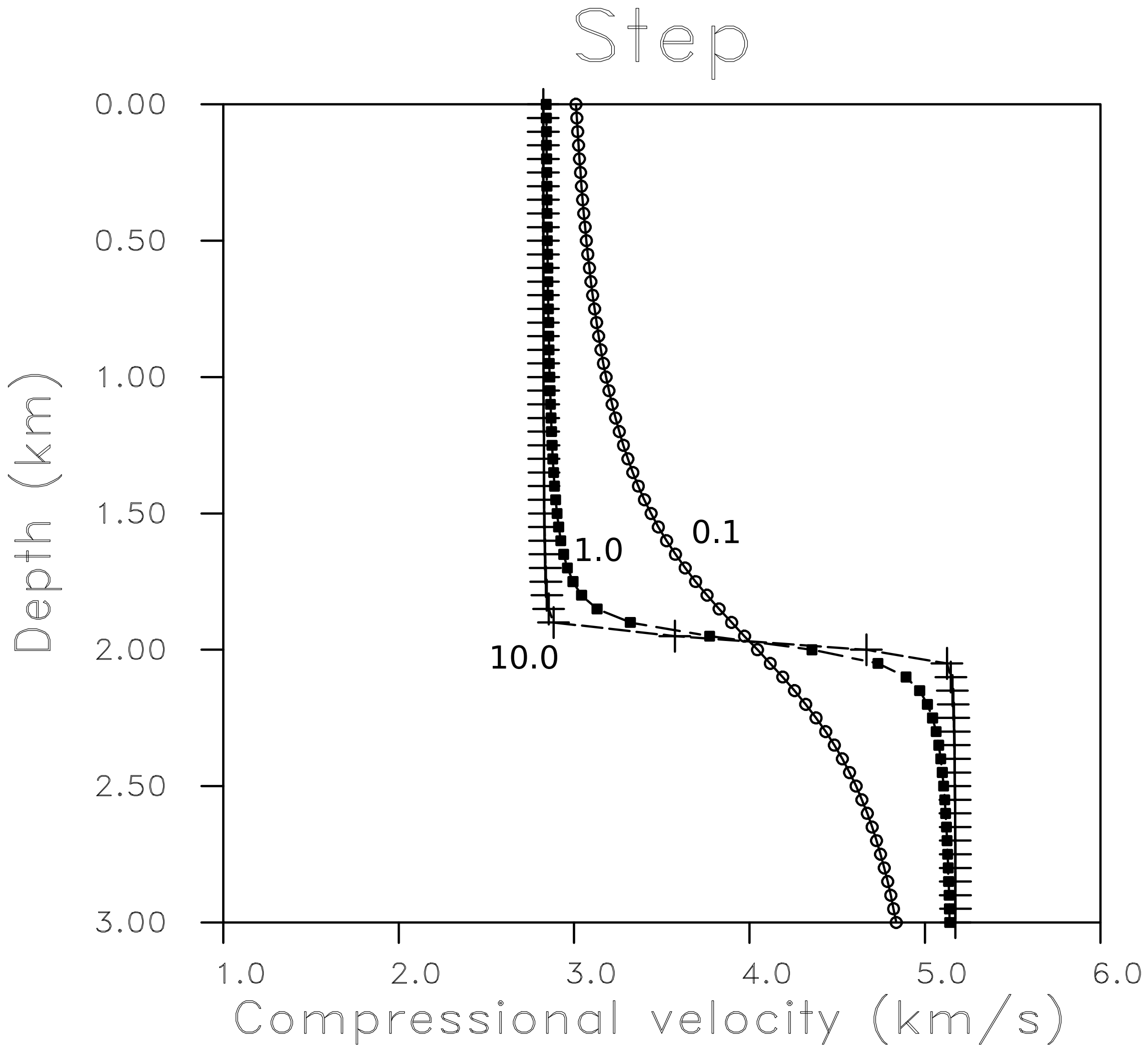

Figure 1. Three depth profiles representing a jump in compressional velocity at a depth of 2.0 km. The depth variations were calculated using equation (38). In this equation a parameter σ determines the transition width of the boundary. Larger values of σ indicate sharper boundaries and the value of σ is indicated for each profile.

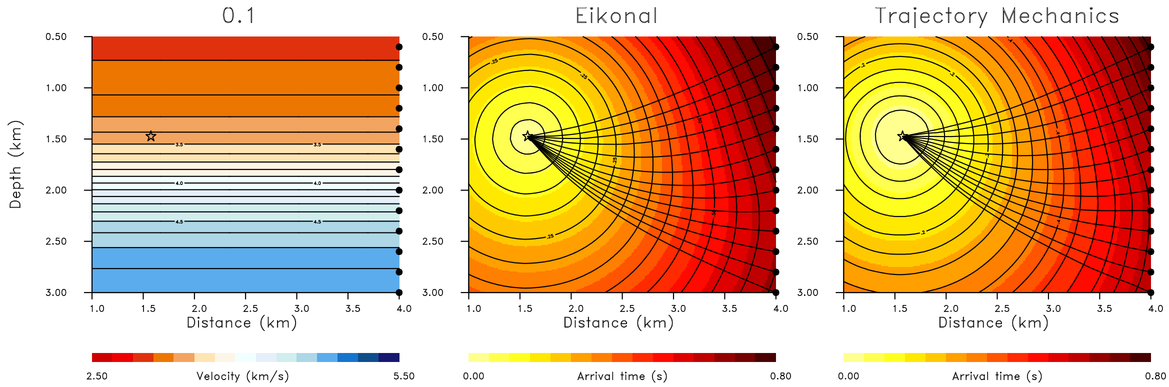

Figure 2. Trajectories associated with a smooth transition in velocity. (Left panel) Vertical slice through the three-dimensional compressional velocity model based upon the function (38) with $\sigma = 0.1$. The source location is indicated by the unfilled star. (Center panel) Ray paths from source to observation points at the right edge of the model, calculated using the eikonal equation. (Right panel) Trajectories based upon travel times estimated from a numerical simulation of a propagating elastic wave and the solution of the differential equation (40). The central frequency of the source-time function used to generate the wavefield is 3.0 Hz.

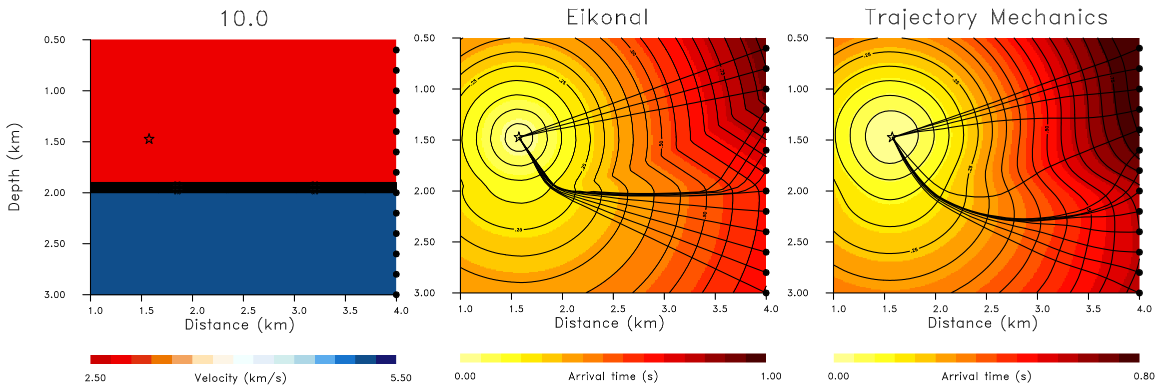

Figure 3. (Left panel) Sharp interface that corresponds to a value of $\sigma = 10.0$ is equation (38). (Center panel) The contours and color variations denote the travel time field obtained by solving the eikonal equation (Zelt and Barton 1998). The ray paths are the solutions of equation (39) and are determined by the gradient of the travel time field. (Right panel) Extended trajectories found by solving equation (40) for each receiver location.

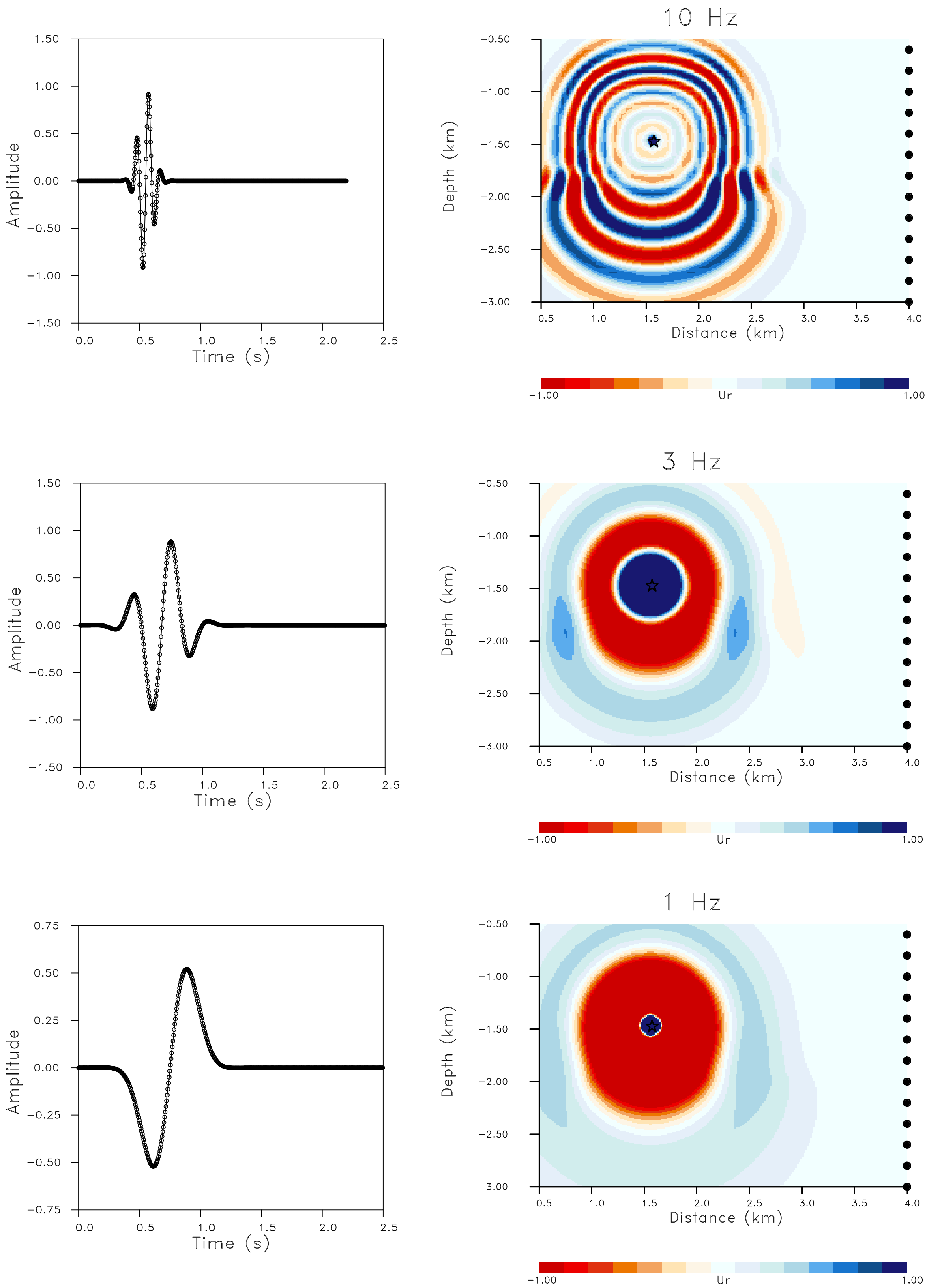

Figure 4. Wavefield snapshots for three different source-time functions. The source-time functions are Gaussian pulses modulated by a sinusoidal oscillation of frequency ω. The left panels depict the source time series while the right panels are vertical cross-sections through wavefield snapshots after 300 time steps. The snapshots are through the source location which is denoted by the unfilled star.

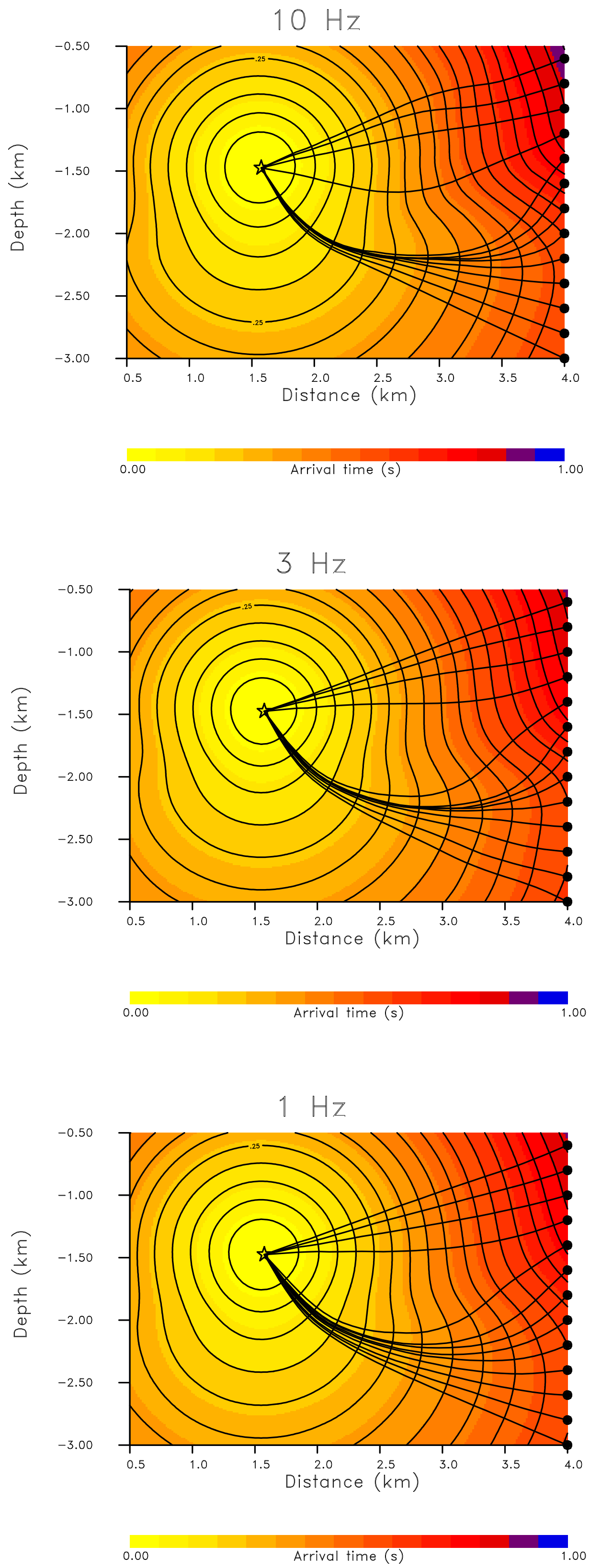

Figure 5. Broad band trajectories for the three frequencies considered in Figure 4. The contour plot denotes the travel time field $T_{num}(\mathbf{x}, \omega)$ and the trajectories are obtained by marching down this gradient.

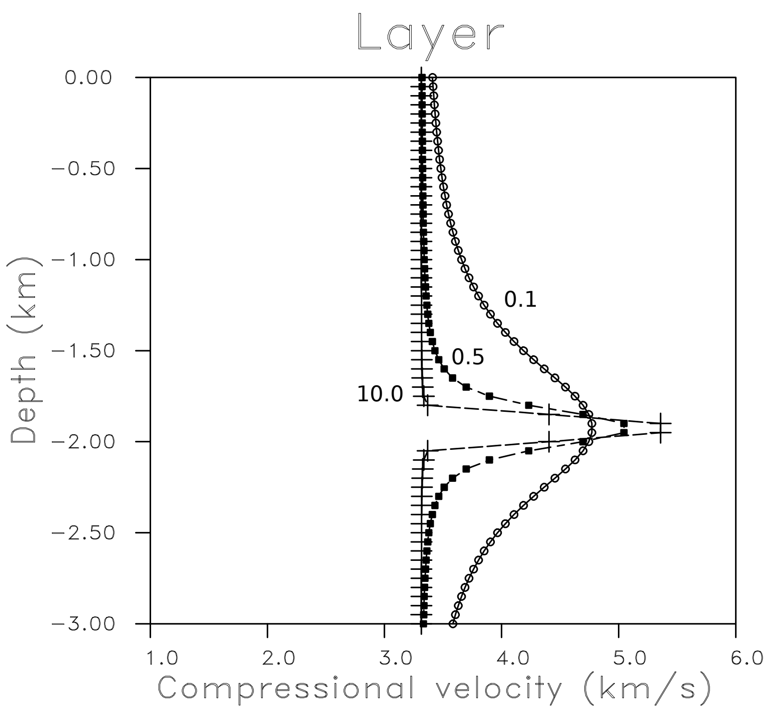

Figure 6. Three depth profiles for layers with boundaries of varying smoothness. The layers are constucted using two interfaces of the form (38) and σ controls the width of the transition. The curves are labeled by their corresponding values of σ.

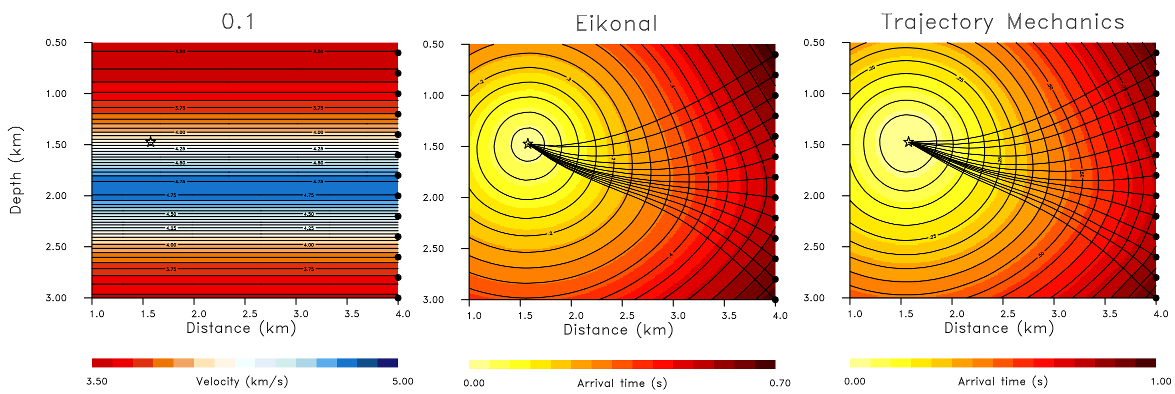

Figure 7. (Left panel) Vertical slice through the three-dimensional layered velocity model generated when $\sigma = 0.1$. (Center panel) Trajectories produced by marching down the gradient of the eikonal equation travel time field. The contours indicate $T_{eikonal}(\mathbf{x})$, the travel times obtained by solving the eikonal equation using the method described in Zelt and Barton (1998). (Right panel) Broad band trajectories obtained by solving equation (40), where the travel time field, indicated by the contours, is from a finite-difference solution of the elasto-dynamic equations of motion.

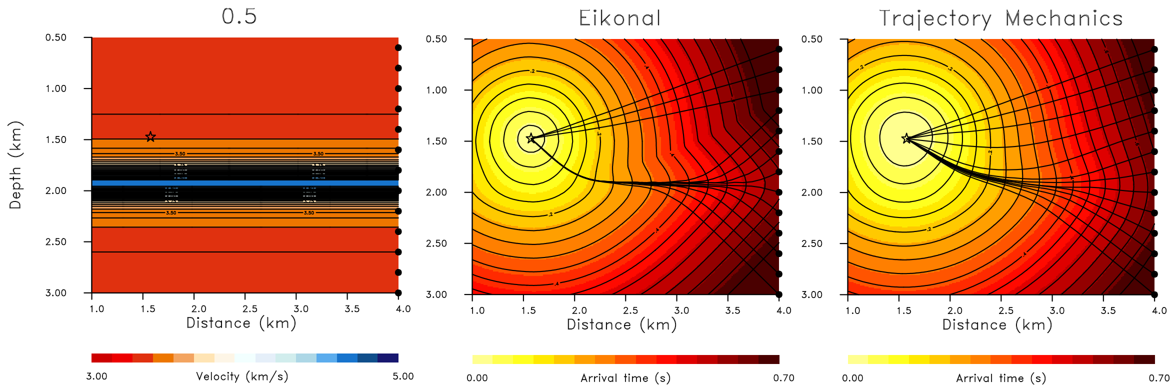

Figure 8. (Left panel) Velocity variation corresponding to a layer with boundaries calculated using equation (38) with $\sigma = 0.5$. (Center panel) Paths based upon the travel times from a solution of the eikonal equation. The travel time field is indicated by the contours and the color variations. (Right panel) Rays derived using the trajectory mechanics approach where equation (40) governs the trajectory geometry and the travel time field is from a numerical solution of equation (1).

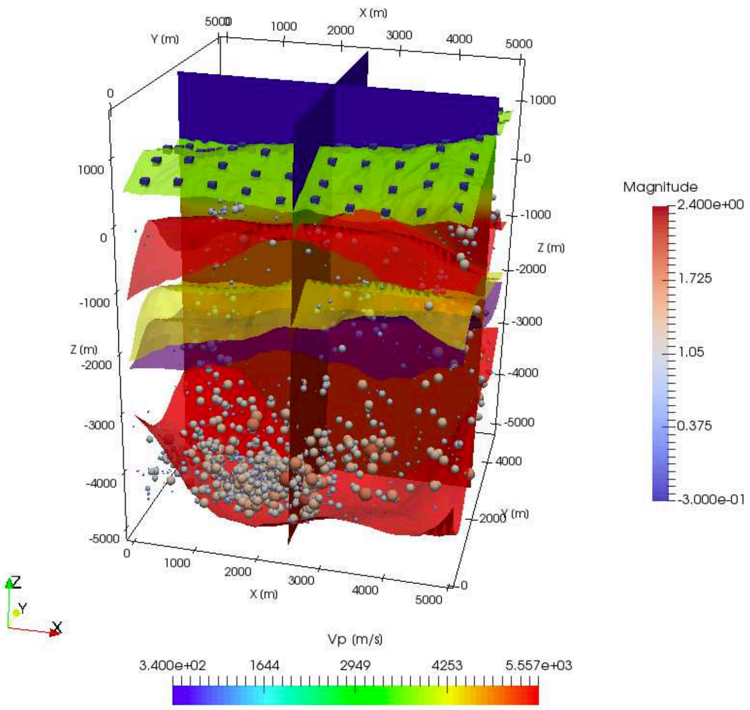

Figure 9. Surfaces defining major lithologic units of a geologic model for a region of the Geysers geothermal field, constructed from a wide variety of data gathered at the Geysers geothermal field (Hartline et al. 2015). Associated seismicity is also plotted as colored spheres, where the radius and color of the sphere indicate the magnitude of the event.

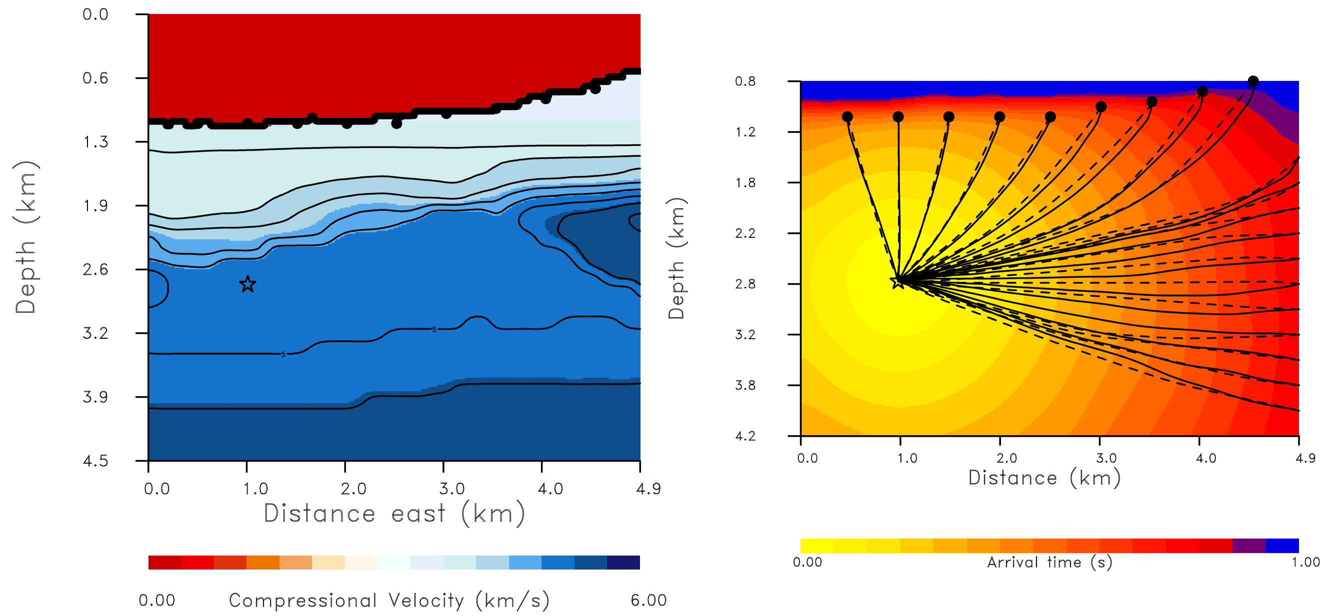

Figure 10. (Left panel) Vertical section through the Geysers velocity model, oriented on an east-west plane through the source point (x, y, z) =(1.0 km, 2.5 km, 2.725 km) which is denoted by the unfilled star. The profile ends at the ground surface though the model does extend 100 m higher with velocities and the density of air. (Right panel) Travel time field from the numerical solution of the elasto-dynamic governing equation (1) along with the broad band trajectories (solid lines). The high frequency trajectories from a solution of the eikonal equation are denoted by the dashed lines.

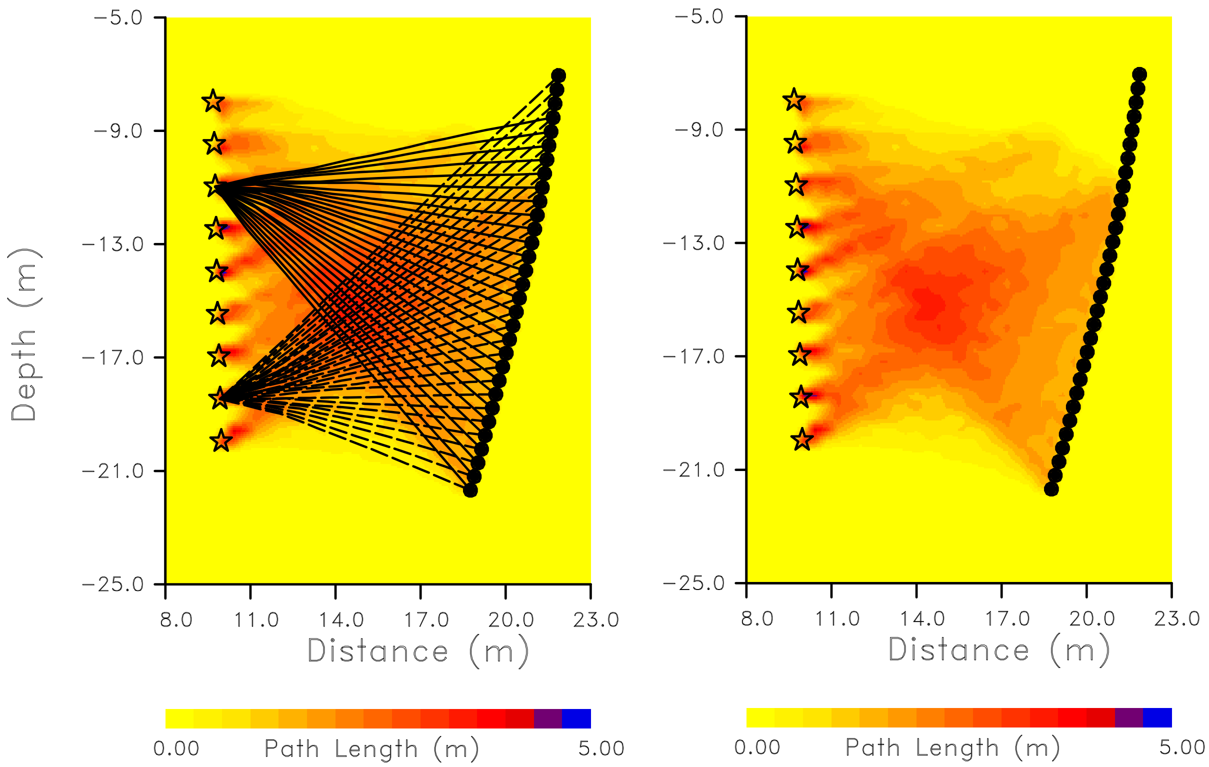

Figure 11. (Left panel) Trajectories for paths between two sources to the active receivers for the Warren Air Force Base crosswell experiment. The sources are denoted by unfilled stars and the receivers by black circles (Right panel) Total path lengths in each cell of the velocity grid used to parameterize the model. The trajectories associated with the final iteration of the imaging algorithm were used to calculate the path lengths.

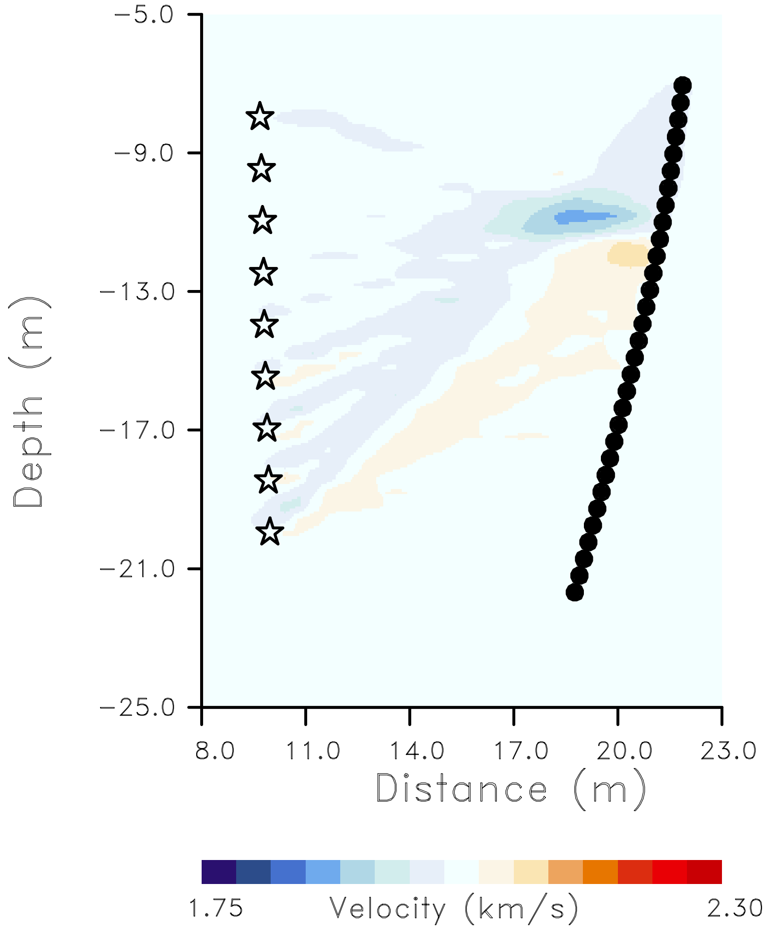

Figure 12. Velocity variations obtained from the tomographic inversion of arrival times from the Warren Air Force Base crosswell experiment. Low velocities due to the injection of fluid into an existing horizontal fracture are evident.